Research Square

Preprints are preliminary reports that have not undergone peer review.
They should not be considered conclusive, used to inform clinical practice,
or referenced by the media as validated information.

Investigation of MHD Flow of a Jeffrey Fluid in microchannel under Slip Conditions

Anil Singh Negi
DIT University
Jogendra Kumar
jogendra.kumar@dituniversity.edu.in

DIT University
Pervinder Singh
DIT University
Dharmendra Tripathi
National Institute of Technology, Uttarakhand

Research Article

Keywords: Jeffrey fluid, magnetohydrodynamics (MHD), squeezing flow, microchannel flow, viscoelastic fluid, slip boundary condition, lubrication theory, micro- and nanofluidics

Posted Date: May 14th, 2026

DOI: https://doi.org/10.21203/rs.3.rs-9414963/v1

License: This work is licensed under a Creative Commons Attribution 4.0 International License.
Read Full License

Additional Declarations: No competing interests reported.

Investigation of MHD Flow of a Jeffrey Fluid in microchannel under Slip Conditions

Anil Sing Negi[1], Jogendra Kumar[1,*], Pervinder Singh[1], Dharmendra Tripathi[2]

[1]*School of Physical Sciences, DIT University, Dehradun, Uttarakhand-248009, India*
[2] *Department of Mathematics, National Institute of Technology, Uttarakhand 246174, India*

Abstract

This work examines the magnetohydrodynamic (MHD) slip flow of Jeffrey fluid confined between a stationary lower plate and a moving upper plate, influenced by a uniform transverse magnetic field. The study highlights the interdependent effects of viscoelasticity, wall motion, magnetic field intensity, and velocity slip on the flow dynamics in a micro-channel. Employing lubrication theory, the governing equations are derived and streamlined to yield analytical expressions for the velocity components, pressure distribution, and volumetric flow rate. The influence of the Jeffrey fluid parameters, which denote relaxation and retardation times, is analyzed in conjunction with magnetic and slip characteristics to clarify deviations from Newtonian behavior. Numerical assessments and graphical outcomes, conducted with MATLAB, demonstrate the interaction of these parameters on flow resistance and pressure gradients. The results yield physical insights pertinent to the regulation and enhancement of MHD-driven viscoelastic microfludic and nanofluidic systems.

Keywords: Jeffrey fluid; magnetohydrodynamics (MHD); squeezing flow; microchannel flow; viscoelastic fluid; slip boundary condition; lubrication theory; micro- and nanofluidics.

1. Introduction

The research study of non-Newtonian fluid dynamics has garnered significant interest owing to its many applications in engineering, biological, and microfluidic systems. The Jeffrey fluid model, among several non-Newtonian models, successfully encapsulates both relaxation and retardation effects, rendering it appropriate for characterizing viscoelastic behavior in polymeric and biological fluids. Comprehending the squeezing flow of these fluids is crucial in the realm of micro- and nanofluidic systems, where fluid movement is frequently restricted between parallel surfaces and affected by slip boundary phenomena.

*Corresponding author: Jogendra Kumar, (publications.jogendra@gmail.com)

The application of an external magnetic field governs the motion of an electrically conducting Jeffrey fluid according to magnetohydrodynamic (MHD) principles. The magnetic field generates Lorentz forces that modify velocity profiles, pressure distributions, and total flow resistance. These interactions are essential in processes involving magnetic control, including drug administration, lab-on-a-chip devices, and lubrication systems.

MHD flows have been extensively studied because of the significance in fluid lubrication theory, micro fludics, and energy systems, as well as biomedical applications. The classical squeeze-flow with parallel plates has been a corner stone in the research of such transports. In the first efforts [1, 2, 3], it was assumed that the MHD squeezing flows leave places in the structure and the rearrangement of the velocity field and the pressure distribution and the distribution of wall shear stresses is altered by the applied magnetic field. Since then, non-Newtonian fluids, specifically Casson and Jeffrey models [5, 11, 25], porous media models [4], and nanofluid models [6, 9] were made and they have been used in the industrial and biomedical applications supported by theoretical analysis.

Further refinements explored additional physical effects, such as thermal radiation and Joule heating [7, 8], chemical reactions and reactive transport [16, 17], and coupled Soret and Dufour diffusion processes [18]. These works highlighted the strong interplay between magnetic forcing, wall motion, and thermal–mass transfer mechanisms, establishing the foundation for more complex microfluidic configurations.

At the microscale, velocity slip and wall shear stress emerge as dominant factors affecting fluid transport. Several studies emphasized slip-flow regimes in MHD and electro-magnetohydrodynamic (EMHD) microchannel flows. Investigations into superhydrophobic slip and temperature jump effects [12], viscous dissipation and micropolar fluids [13], and Hall/ion-slip current influences [14] have revealed significant modifications in pressure gradients and velocity profiles. EMHD studies extended these findings to fractional viscoelastic fluids [19], microchannels with random roughness [22], and porous geometries with melting and slip conditions [23]. Reviews of EMHD transport mechanisms in microchannels [21] further stress the importance of incorporating electrokinetic effects in next-generation microfluidic designs.

Recent efforts have advanced the analysis of MHD slip flows in open-ended vertical microchannels [24], entropy generation and thermosolutal transport in inclined microchannels [26], and electro-osmotic flows with wall motion [27], all reinforcing the growing demand for accurate models that couple wall-driven motion, slip, and magnetic fields. Complementary contributions include studies of bio-thermal convection with multiple slip conditions [20], stability analysis of dual slip solutions [9, 10], and entropy-based optimization strategies for transport enhancement [28].

Despite this progress, the combined influence of wall squeezing motion, velocity slip, and transverse magnetic fields on electrolyte flows in microchannels remains incompletely resolved.

This study examines the synergistic effects of magnetohydrodynamic forces, wall compression motion, and slip boundary conditions on the flow characteristics of a Jeffrey fluid in a microchannel. Utilizing lubrication theory, analytical formulas are derived for the principal flow parameters, and the effects of dimensionless quantities, including the Jeffrey number, Hartmann number, and slip parameters, are thoroughly analyzed. The results not only enhance standard Newtonian squeezing flow theory but also offer novel insights into the tunability of viscoelastic magnetohydrodynamic flows for sophisticated microfluidic applications.

2. Formulation of the Problem

This model examines the influence of a magnetic field on the non-Newtonian fluid flow between two infinitely long parallel plates, incorporating the slip effect. In geometry, the lower plate (W_1) remains stable, while the top plate (W_2) undergoes continuous compression and expansion, with the compression and expansion zone ranging from $\frac{W}{2}$ to W. The reference geometry is depicted as a two-dimensional (x, y) channel in Figure 1. The separation between parallel plates is represented by W, while the length of the plates is indicated by L, with the condition that $W << L$ holds true. The fluid's input and outlet pumping flow is induced by the compression and expansion of the upper wall.

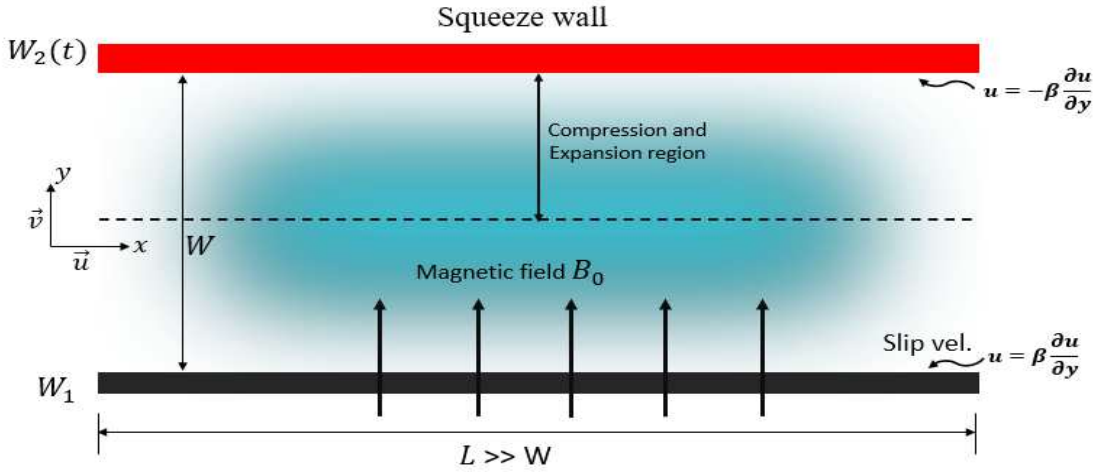

Figure 1: Schematic illustration of the squeeze flow regime of the slip effect as well as the magnetic effect during compression and expansion within a microchannel.

When the lower wall has been fixed, picture a compressive action of the top wall, which delineates the subsequent profile:

$$W_1 = -\frac{1}{2}. \tag{1}$$

$$W_2(x,t) = \frac{1}{4}(1 + cos(2\pi t S_t)). \tag{2}$$

2.1. Model Definition

Since Jeffrey fluid has been considered in the study, hence a constitutive equation for the stress $\bar{\tau}$ will be a crucial part of the governing equations for the model:

$$\bar{\tau} = \frac{\mu}{1+\lambda_1}(\dot{\gamma} + \lambda_2 \ddot{\gamma}). \tag{3}$$

where λ_1, λ_2, $\dot{\gamma}$, and μ are ratio of relaxation to retardation times, the rate of strain, viscosity, and dots represents the derivative with respect to time.
The simplified form of the equation (3) is given by:

$$\bar{\tau}_{\bar{x}\bar{y}} = \frac{\mu}{1+\lambda_1}\left[1 + \lambda_1\left(\bar{u}\frac{\partial}{\partial \bar{x}} + \bar{v}\frac{\partial}{\partial \bar{y}}\right)\right]\left(\frac{\partial \bar{v}}{\partial \bar{x}} + \frac{\partial \bar{u}}{\partial \bar{y}}\right). \tag{4}$$

2.2. Governing Equations

In the presence of a static magnetic field oriented transversely, the subsequent governing equations pertaining to two-dimensional unsteady incompressible fluid flow are:

$$\frac{\partial \bar{u}}{\partial \bar{x}} + \frac{\partial \bar{v}}{\partial \bar{y}} = 0, \tag{5}$$

$$\rho\left(\frac{\partial \bar{u}}{\partial \bar{t}} + \bar{u}\frac{\partial \bar{u}}{\partial \bar{x}} + \bar{v}\frac{\partial \bar{u}}{\partial \bar{y}}\right) = -\frac{\partial \bar{p}}{\partial \bar{x}} + \frac{\partial \bar{\tau}_{\bar{x}\bar{x}}}{\partial \bar{x}} + \frac{\partial \bar{\tau}_{\bar{x}\bar{y}}}{\partial \bar{y}} - \sigma B_0^2 \bar{u}, \tag{6}$$

$$\rho\left(\frac{\partial \bar{v}}{\partial \bar{t}} + \bar{u}\frac{\partial \bar{v}}{\partial \bar{x}} + \bar{v}\frac{\partial \bar{v}}{\partial \bar{y}}\right) = -\frac{\partial \bar{p}}{\partial \bar{x}} + \frac{\partial \bar{\tau}_{\bar{y}\bar{x}}}{\partial \bar{x}} + \frac{\partial \bar{\tau}_{\bar{y}\bar{y}}}{\partial \bar{y}}, \tag{7}$$

where, $\bar{u}$ and $\bar{v}$ represent the velocities in the $\bar{x}$ and $\bar{y}$ directions, respectively. The other parameters are defined as follows: ρ is the density, t is time, p is pressure, β_0 is the magnetic field and $\bar{\tau}_{\bar{x}\bar{x}}$, $\bar{\tau}_{\bar{x}\bar{y}}$, $\bar{\tau}_{\bar{y}\bar{x}}$,

2.3. Dimension analysis

Using the following transformations, the equations (5-7) have been no-dimensionalise :

$$\begin{gathered} x = \frac{\bar{x}}{L}, \quad y = \frac{\bar{y}}{W}, \quad W_1 = \frac{\bar{W}_1}{W}, \quad W_2(t) = \frac{\bar{W}_2(t)}{W}, \quad t = \frac{u_0 \bar{t}}{L}, \\ u = \frac{\bar{u}}{u_0}, \quad v = \frac{\bar{v}}{u_0 \delta}, \quad p = \frac{W^2 \bar{p}}{\mu u_0 L}, \quad \tau = \frac{W \bar{\tau}}{u_0}, \quad Ha = \beta_0 W \sqrt{\frac{\sigma}{\mu}}. \end{gathered} \tag{8}$$

where u_0 denotes the reference velocity. The resulting equations for incompressible fluid at low Reynolds number $\left(\frac{u_0 W \rho}{\mu} \rightarrow 0\right)$ and influenced by $\delta = W/L << 1$, in the presence of a transverse magnetic field, are as follows:

$$\frac{\partial u}{\partial x} + \frac{\partial v}{\partial y} = 0, \tag{9}$$

$$-\frac{\partial p}{\partial x} + \frac{1}{1+\lambda_1}\frac{\partial^2 u}{\partial y^2} - Ha^2 u = 0, \tag{10}$$

$$\frac{\partial p}{\partial y} = 0. \tag{11}$$

where Ha is the magnetic field parameter (Hartman Number).

The following no-slip boundary conditions are applied together with wall conditions (1-2):

$$u|_{y=W_1} = \beta \frac{\partial u}{\partial y} \quad \text{and} \quad u|_{y=W_2(t)} = -\beta \frac{\partial u}{\partial y}. \tag{12}$$

2.4. Analytical Solutions

$p = p(x,t)$, as indicated by equation (11), signifies that the static pressure varies solely in the axial direction and remains uniform in the vertical direction. Thus, the axial velocity component can be derived by performing two integrations of equation (10) with the corresponding boundary condition (12), and demonstrated as below:

$$\begin{aligned} u = \frac{1}{Ha^2}\frac{\partial p}{\partial x}\Bigg[-1 - \frac{\beta K cosh\Big\{\frac{K}{2}(W_1 - W_2)\Big\} - sinh\Big\{\frac{K}{2}(W_1 - W_2)\Big\}}{sinh\Big\{K(W_1 - W_2)\Big\}(1+\beta^2 K^2) - \beta K cosh\Big\{K(W_1 - W_2)\Big\}} \\ \Big\{2cosh\Big\{\frac{K}{2}(2y - W_1 - W_2)\Big\}\Big\}\Bigg]. \end{aligned} \tag{13}$$

Where $K = Ha\sqrt{1+\lambda_1}$.

The transverse velocity can be computed using the continuity equation (9).

$$v = \frac{1}{Ha^2}\frac{\partial^2 p}{\partial x^2}\Bigg[(y - W_1) + \frac{\beta cosh\Big\{\frac{K}{2}(W_1 - W_2)\Big\} - \frac{2}{K}sinh\Big\{\frac{K}{2}(W_1 - W_2)\Big\}}{sinh\Big\{K(W_1 - W_2)\Big\}(1 + \beta^2K^2) - \beta K cosh\Big\{K(W_1 - W_2)\Big\}} \Big\{sinh\Big\{\frac{K}{2}(2y - W_1 - W_2)\Big\} - sinh\Big\{\frac{K}{2}(W_1 - W_2)\Big\}\Big\}\Bigg]. \tag{14}$$

Since $v|_{y=W_2} = \frac{\partial W_2}{\partial t}$ establishes a correlation between the temporal rate of change of the channel wall $\left(\frac{\partial W_2}{\partial t}\right)$ and the axial pressure gradient $\frac{\partial p}{\partial x}$, it yields

$$\frac{\partial W_2}{\partial t} = \frac{1}{Ha^2}\frac{\partial^2 p}{\partial x^2}\Bigg[\Big\{(W_2 - W_1)\Big\} - \frac{\beta cosh\Big\{\frac{K}{2}(W_1 - W_2)\Big\} - \frac{2}{K}sinh\Big\{\frac{K}{2}(W_1 - W_2)\Big\}}{sinh\Big\{K(W_1 - W_2)\Big\}(1 + \beta^2K^2) - \beta K cosh\Big\{K(W_1 - W_2)\Big\}} \Big\{2sinh\Big\{\frac{K}{2}(W_1 - W_2)\Big\}\Big\}\Bigg]. \tag{15}$$

The pressure gradient in the axial direction can be obtained by separating the terms and integrating with respect to x.

$$\frac{\partial p}{\partial x} = \frac{\Delta p}{L} + \frac{Ha^2\frac{\partial W_2}{\partial t}(2x - L)}{2\Bigg[\Big\{(W_2 - W_1)\Big\} - \frac{\beta cosh\Big\{\frac{K}{2}(W_1 - W_2)\Big\} - \frac{2}{K}sinh\Big\{\frac{K}{2}(W_1 - W_2)\Big\}}{sinh\Big\{K(W_1 - W_2)\Big\}(1 + \beta^2K^2) - \beta K cosh\Big\{K(W_1 - W_2)\Big\}} \Big\{2sinh\Big\{\frac{K}{2}(W_1 - W_2)\Big\}\Big\}\Bigg]}. \tag{16}$$

Moreover, the expression for the shear-stress distribution can be derived as:

$$\tau = \delta^2\frac{\partial v}{\partial x} + \frac{\partial u}{\partial y} \cong \frac{\partial u}{\partial y}. \tag{17}$$

This is derived by calculating the derivative of the axial velocity and expressing it as:

$$\tau = -\frac{1}{Ha^2}\frac{\partial p}{\partial x}\Bigg[\frac{\beta K cosh\Big\{\frac{K}{2}(W_1 - W_2)\Big\} - sinh\Big\{\frac{k}{2}(W_1 - W_2)\Big\}}{sinh\Big\{k(W_1 - W_2)\Big\}(1 + \beta^2k^2) - \beta k cosh\Big\{k(W_1 - W_2)\Big\}} \Big\{2K sinh\Big\{\frac{k}{2}(2y - W_1 - W_2)\Big\}\Big\}\Bigg]. \tag{18}$$

After obtaining the velocity components, one may use the conventional connection $u = \frac{\partial \psi}{\partial y}$ and $v = -\frac{\partial \psi}{\partial x}$. to get an expression for the velocity stream-function $\psi(x, y, t)$. This deduced expression

is as follows:

$$\psi = -\frac{1}{Ha^2}\frac{\partial p}{\partial x}\Bigg[(y - W_1) - \frac{\frac{2}{K}\Big\{\beta K cosh\Big\{\frac{K}{2}(W_1 - W_2)\Big\} - sinh\Big\{\frac{K}{2}(W_1 - W_2)\Big\}\Big\}}{sinh\Big\{K(W_1 - W_2)\Big\}(1 + \beta^2 K^2) - \beta K cosh\Big\{K(W_1 - W_2)\Big\}} \\ \Big\{sinh\Big\{\frac{K}{2}(W_1 - W_2)\Big\} - sinh\Big\{\frac{K}{2}(2y - W_1 - W_2)\Big\}\Big\}\Bigg]. \tag{19}$$

Lastly, the flow rate (Q), can also be expressed and evaluated as

$$Q = \int_{W_1}^{W_2} u(x, y, t)dy, \tag{20}$$

$$Q = \frac{1}{Ha^2}\frac{\partial p}{\partial x}\Bigg[(W_1 - W_2) - \frac{\beta K cosh\Big\{\frac{K}{2}(W_1 - W_2)\Big\} - sinh\Big\{\frac{K}{2}(W_1 - W_2)\Big\}}{sinh\Big\{K(W_1 - W_2)\Big\}(1 + \beta^2 K^2) - \beta K cosh\Big\{K(W_1 - W_2)\Big\}} \\ \Big\{\frac{4}{K} sinh\Big\{\frac{K}{2}(W_2 - W_1)\Big\}\Big\}\Bigg]. \tag{21}$$

3. Results and Discussion

This section of the study will investigate the behavior of Jeffery fluid flow in the presence of a magnetic field between parallel plates. The governing equations are solved analytically, and MATLAB software is used to generate graphs and evaluate the effects of physical parameters Hartmann number (Ha), slip parameter (β) and Jeffery fluid parameter (λ_1).

Fig.2 illustrates the evolution of axial velocity, vertical velocity, and shear stress along the vertical coordinate y for a complete cycle of squeezing plates i.e, for $T \in [0, 1]$. These results are obtained for the Hartmann number $Ha = 5$, slip parameter $\beta = 0.1$, Jeffrey fluid parameter $\lambda = 1$ at $x = 0.25$.

The Fig.(2a) represents the axial velocity u profiles at different time levels over one complete oscillation cycle. A straight-line velocity distribution is observed at $t = 0$, 0.5 , 1, indicating symmetric states of the flow at the beginning, midpoint, and end of the cycle. During the compression phase, the velocity profiles bend towards the left side, indicating a predominantly negative axial velocity near the upper region. As time increases from $t \in [0, 0.5]$, the magnitude of the negative velocity increases, suggesting that the squeezing upper wall strengthens the downward flow. The curvature of the profiles increases with time, showing enhanced shear near the boundaries and a stronger compressive effect. n the expansion phase, the profiles shift to the right side, indicating positive axial velocity as the wall moves upward. Starting from $t \in [0.5, 1]$, the flow gradually

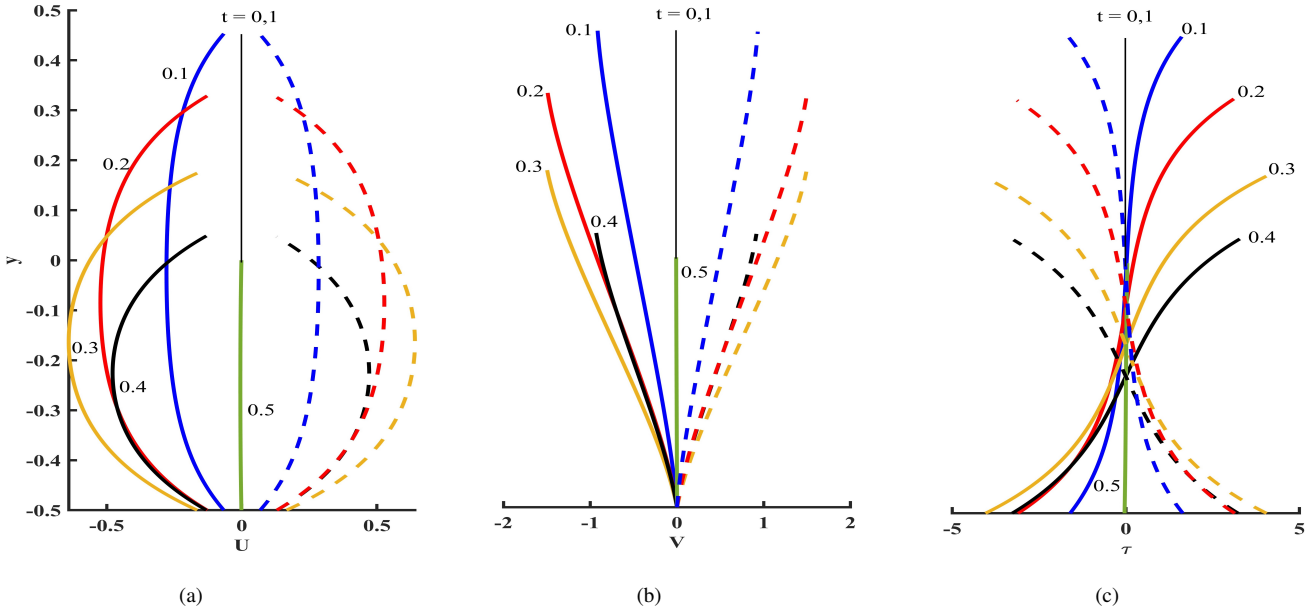

Figure 2: Time trace of the axial velocity u, the vertical velocity v, and the shear stress τ for one complete cycle $T = 1$, caused by the motion of the squeezing upper wall as a function of the vertical direction y for $\lambda = 1$, $\beta = 0.1$ and $Ha = 5$.

accelerates upward, with the velocity magnitude increasing as $t \to 1$. The right-inclined profiles confirm the dominance of the expansion (stretching) effect, leading to an opposite but symmetric flow pattern compared to the compression stage.

Fig.(2c) illustrates the physical behaviour of the squeeze flow during both the compression and expansion phases. On the left side, the compression phase is shown, where the upper plate moves downward, causing an increase in pressure and a strong negative shear stress. This indicates that the fluid layers slide rapidly over each other, leading to a higher viscous resistance. As time progresses, the compression weakens, and therefore the intensity of shear stress and the velocity gradients decrease. On the right side, the expansion phase is depicted, where the upper plate moves upward and the fluid expands, resulting in a positive shear stress which reflects the stretching between fluid layers. With increasing time, the expansion becomes slower, and the stress profiles gradually flatten.

Fig.(3a) displays the axial velocity for various Hartmann number values. The axial velocity exhibits a parabolic shape, reaching its highest value near the center of both walls. For the minimal Hartmann number, $Ha = 5$, the magnitude of the axial velocity is maximum, and for the maximum value, $Ha = 20$, it is minimum. In other words, the parabolic shape between the walls steadily diminishes with increasing Hartmann number, indicating that axial velocity decreases with in-

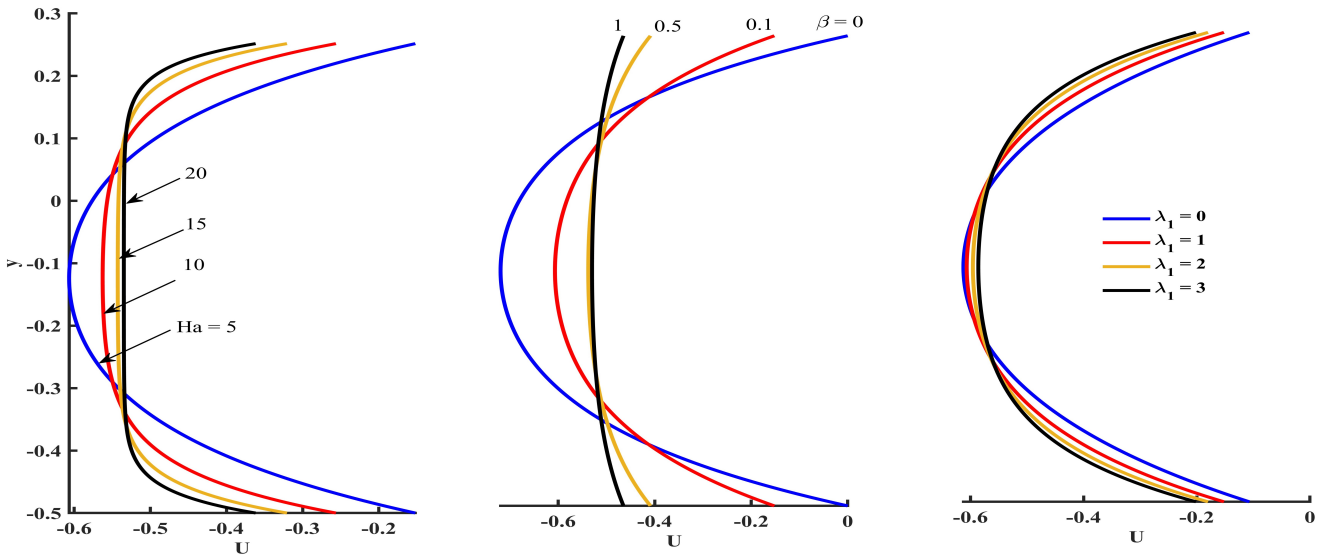

(a) (b) (c)

Figure 3: The axial velocity u distribution as a function of the vertical direction y. The results are given for various values of (a) Hartmann number Ha, (b) slip values β, and (c) Jeffery fluid parameter λ_1 presented at a time snapshot $t = 0.25$ in compression phase.

creasing Hartmann number. Since the Lorentz force acts as a damper, reducing the fluid's velocity, the application of a magnetic field allows for the control of fluid flow. Fig.(3b) presents the axial velocity profiles for various values of the slip parameter β at a fixed Hartmann number $Ha = 5$ during the compression phase. Introducing a slip at the walls reduces the near-wall friction, thereby allowing more fluid momentum to develop. As shown in the figure, when $\beta = 0$ (no-slip condition), the axial velocity at the walls is zero. However, as the slip parameter β increases, the wall velocity becomes positive and increases accordingly. Furthermore, Figure 3(b) demonstrates that increasing the slip parameter β leads to a reduction in the axial velocity magnitude at the center of the channel, indicating that the slip effect redistributes the velocity profile by enhancing near-wall motion while slightly suppressing the core flow.

Fig.(3c) demonstrates that during the compression phase, at a particular time and position, altering the Jeffrey fluid parameter λ_1 considerably modifies the axial velocity for a Hartmann number $Ha = 5$. In general, increasing the value of the Jeffrey fluid parameter λ_1 results in increased axial velocity u and reaching its highest value near the center of the channel. The Jeffrey fluid parameter is a direct measure of the fluid's viscoelastic memory, allowing for greater velocity variations. Physically, the Jeffrey fluid parameter quantifies the fluid's viscoelastic qualities, which influence its response to driving force.

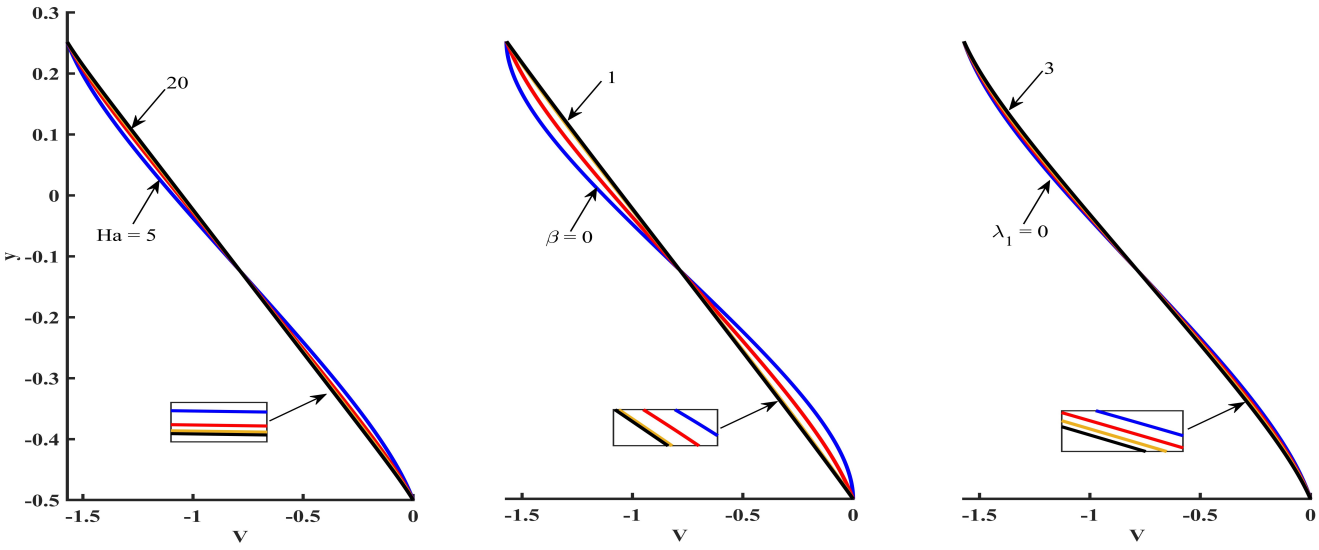

(a) (b) (c)

Figure 4: Variations in the transverse velocity profile V at time snapshots $t = T/4$ at a fixed location $x = 0.25$ for various values of the Hartmann number Ha, the slip parameter β, and the Jeffery fluid parameter λ_1.

Fig.(4a) illustrates the vertical velocity profile at the fixed streamwise location $x = 0.25$ for different values of the Ha. As the Hartmann number increases, the magnitude of the v decreases, which indicates the damping effect of the applied magnetic field on the flow. Higher values of Ha produce steeper gradients near the walls, reflecting the formation of a Hartmann boundary layer, while the core region of the flow becomes comparatively flatter. The variation among the curves is moderate, showing that at this particular location the magnetic influence is noticeable but not extremely dominant. Physically, this behaviour demonstrates that the magnetohydrodynamic effects suppress the shear and flatten the velocity distribution, thereby stabilizing the flow.

Fig.(4b) presents the vertical velocity profile v for different values of the slip parameter β. As β increases, the slip at the wall becomes stronger, which slightly reduces the magnitude of the velocity and makes the profile smoother. For $\beta = 0$ (the no-slip condition), the velocity changes more sharply near the wall, whereas for $\beta > 0$, the relative motion between the fluid layers decreases, leading to a reduction in shear. The magnified view in the lower region clearly shows that the velocity gradient becomes smaller as β increases, indicating a reduction in flow resistance. In summary, an increase in the slip parameter results in a more uniform and less steep vertical velocity profile, demonstrating the weakening influence of wall friction on the flow.

Fig.(4c) illustrates the variation of the vertical velocity v for different values of the Jeffrey fluid parameter λ_1. As λ_1 increases, the influence of fluid elasticity becomes more pronounced, which

slightly reduces the magnitude of the vertical velocity throughout the domain. For $\lambda_1 = 0$, the behaviour corresponds to a standard Newtonian fluid, showing a steeper velocity gradient near the wall. When $\lambda_1 > 0$, the elastic response of the Jeffrey fluid weakens the rate of deformation, leading to a smoother and less steep velocity profile. The magnified region highlights that the velocity profiles separate more clearly as λ_1 increases, indicating increased resistance to rapid changes in motion. Overall, increasing λ_1 enhances the elastic effects in the fluid, thereby reducing shear and moderating the vertical velocity distribution.

Fig.(5) illustrates how the Hartmann number Ha, slip parameter β, and Jeffrey fluid parameter λ_1 affect the change of shear stress τ in the transverse direction y between parallel plates. Fig.(5a) depicts the shear stress τ along the transverse coordinate y in MHD flow. The graph depicts various Hartmann number curves (i.e., $Ha = 5, 10, 15, 20$), which clearly show that as the Hartmann number increases, the magnitude of shear stress decreases significantly in the entire flow region. This is because when the Lorentz force is high, the motion of the fluid is significantly damped, resulting in a decrease in the gradient of axial velocity, which in turn reduces the shear stress. The figure also shows a sharp change in shear stress near the walls, whereas in the middle region of the channel, all of the curves show comparatively more flattening, i.e. as the Hartmann number increases, the resistance to flow increases, and as a result, the magnitude of shear stress decreases in the entire region, which is a characteristic phenomenon of MHD flow. The curves in Fig.(5b) show that as the slip parameter β increases, the shear stress gradually decreases throughout the flow region. This is due to the increased relative motion between the fluid and the solid surface, which reduces the velocity gradient and thus the shear stress. As the slip parameter increases (i.e $\beta = 0; 0.01; 0.05; 0.09$), the shear stress falls monotonically. This is because the rise in slip parameter lessens the viscous shear acting on the flow, resulting in a drop in the magnitude of shear stress across the flow region. Fig.(5c) demonstrates that increasing the Jeffrey fluid parameter λ_1 reduces wall shear stress due to the viscoelastic nature of the Jeffrey fluid. The curves clearly illustrate that shear stress is 0 in the center of the channel and gradually decreases near the walls.

Fig.(6a) illustrates the influence of the Hartmann number Ha on the axial pressure difference Δp. It is clearly observed that the magnitude of Δp increases significantly with an increase in Ha. Physically, a higher Hartmann number corresponds to a stronger magnetic field, which enhances the Lorentz force acting opposite to the fluid motion. This magnetic resistance suppresses the velocity field, thereby requiring a larger pressure gradient to sustain the flow between the plates. Consequently, the peak pressure difference rises sharply as Ha increases, which is consistent with the fundamental behavior of magnetohydrodynamic (MHD) flows where the magnetic field acts as an effective resistive force.

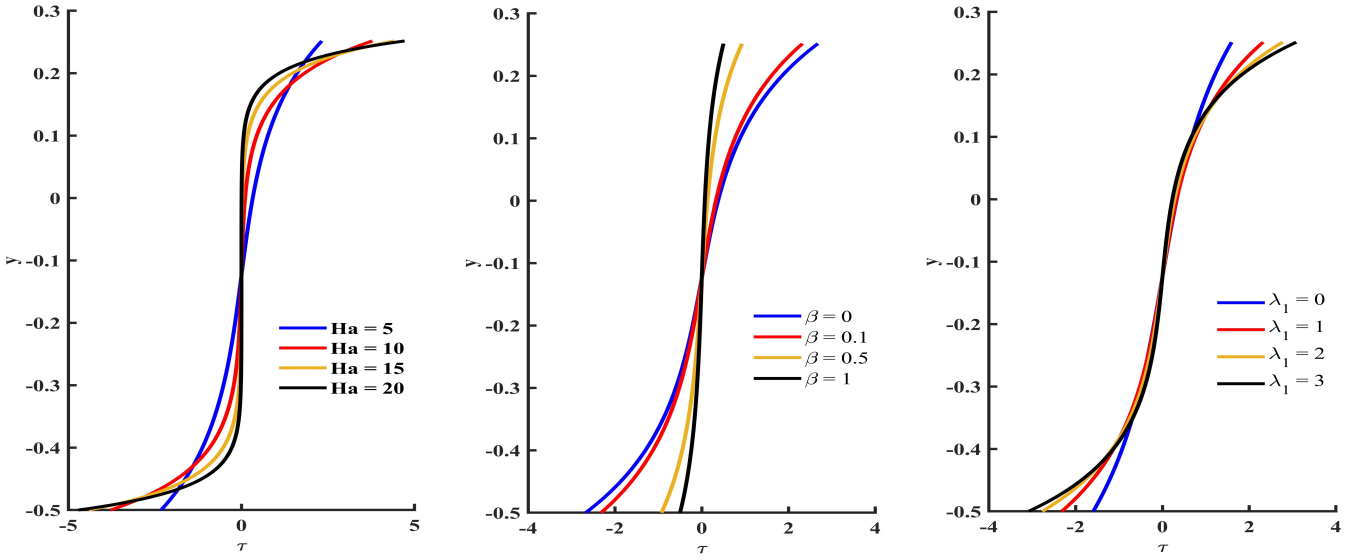

(a) (b) (c)

Figure 5: The figure shows the shear stress τ distribution versus the vertical direction y. The results are given at time snapshots $t = T/4$ in the compression phase for different values of (a) the Hartmann number Ha, (b) the slip parameter β, and (c) the Jeffrey fluid parameter λ_1.

Fig.(6b) presents the effect of the slip parameter β on the pressure distribution. As β increases, the pressure difference profile shifts upward, resulting in a noticeable increase in the peak value of Δp. Physically, the slip parameter accounts for the degree of fluid–surface slip, and a higher value implies reduced no-slip resistance at the wall. Although the wall shear stress decreases due to slip, the effective pressure difference needed to maintain the same flow rate becomes larger. This behavior indicates that slip conditions modify the momentum transfer at the boundaries, making the pressure-driven flow more sensitive to variations in β.

Fig.(6c) depicts the variation in Δp with respect to the Jeffery fluid parameter λ_1. An increase in λ_1 leads to a substantial rise in the peak pressure difference. The parameter λ_1 characterizes the elastic and relaxation properties of the Jeffery fluid. As λ_1 grows, the fluid exhibits stronger elastic effects, thereby increasing the internal structural stresses in the flow domain. To overcome these additional stresses and sustain the axial motion, a higher pressure gradient becomes necessary. In contrast, the Newtonian case ($\lambda_1 = 0$) yields comparatively lower pressure differences, confirming the significant role of fluid elasticity in governing the pressure distribution.

Overall, fig.(6) demonstrate that the axial pressure distribution is highly sensitive to variations in magnetic field strength, slip conditions, and fluid elasticity. Each parameter introduces distinct physical mechanisms-magnetic resistance, surface slip, and elastic stress-that substantially modify

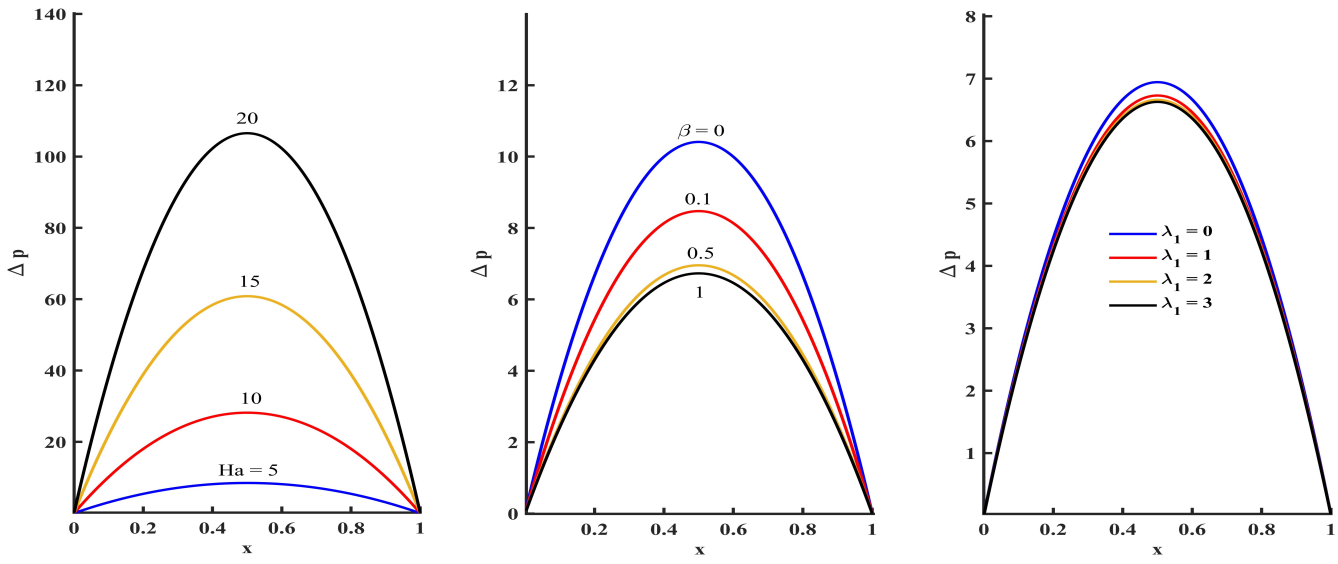

(a) (b) (c)

Figure 6: The effect of the (a) Hartmann number Ha, (b) slip parameter β and (c) Jeffery fluid parameter λ_1 on axial pressure distribution. The results are computed for $x = 0.25$, and at time $t = T/4 = 0.25$.

the pressure field in the system.

Fig.(7a) displays the axial pressure gradient for various Hartmann numbers Ha. The results reveal that as Ha increases, the amplitude of the pressure gradient also increases, with a positive value in the first half of the channel and a negative value in the second half. The pressure gradient is lowest at $Ha = 5$. As Ha rises to $10, 15$, and 20, magnetic damping increases dramatically, demanding a greater pressure gradient to maintain flow speed. Thus, Fig.(7a) clearly indicates that the pressure gradient increases extremely sensitively with increasing Ha, and the magnetic field in the fluid plays an important role in controlling pressure-driven flow. Fig.(7b) & (7c) shows that slip parameter β and the Jeffrey fluid parameter λ_1 behave similarly with the pressure gradient. However, the influence is least for β and most evident for λ_1. This picture indicates that the pressure gradient grows with increasing values of the Hartmann number Ha, slip parameter β, and Jeffrey fluid parameter (λ_1).

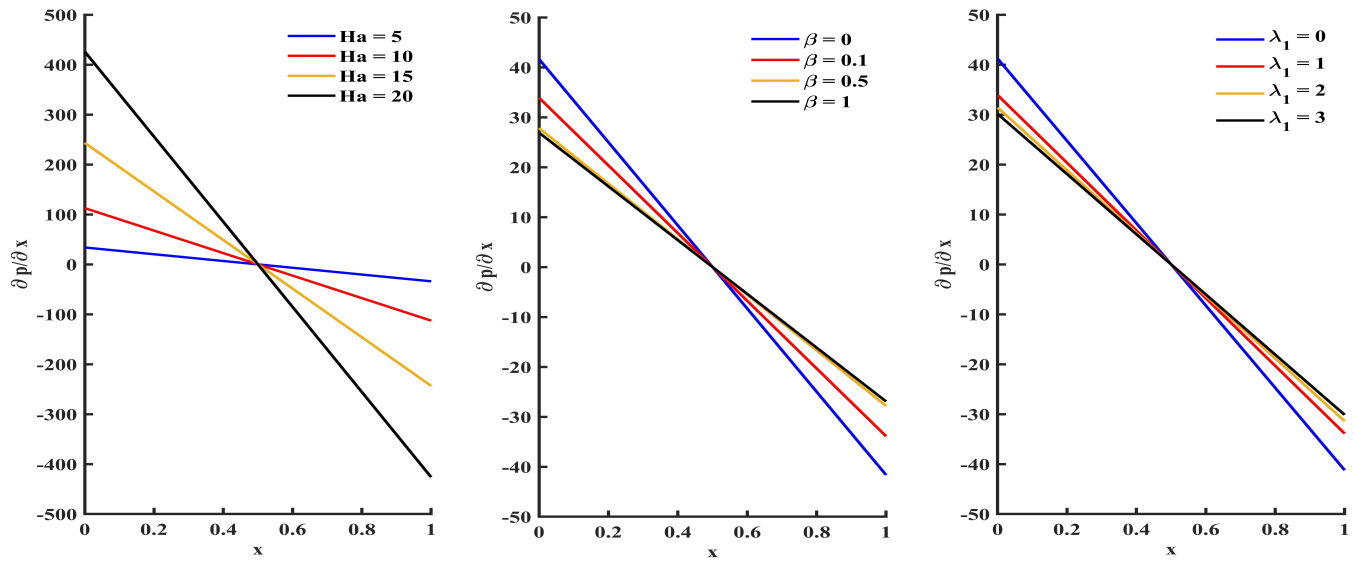

(a) (b) (c)

Figure 7: The pressure gradient for different value of (a) Hartmann number Ha, (b) slip parameter β and (c) Jeffery fluid parameter λ_1 at the compression phase with fixed values $x = 0.25$, and time $t = T/4$.

Fig.(8) illustrates the variation of the volumetric flow rate Q at a fixed axial location $x = 0.25$ and fixed time $T = 0.25$ (compression phase) for different values of (a) the Hartmann number Ha, (b) the slip parameter β, and (c) the Jeffery fluid parameter λ_1. The physical interpretation of these effects is discussed below.

From Fig.(8a), it is observed that the volumetric flow rate Q decreases with an increase in the Hartmann number Ha. It mean that as magnetic field intensity increases (Ha), a magnetic force is generated within the electrically conducting fluid, which acts opposite to the direction of motion. This resistive force suppresses the fluid velocity and consequently reduces the volumetric flow rate. Hence, higher values of Ha indicate stronger magnetic damping, leading to a more restrained flow.

Fig.(8b) shows that the volumetric flow rate Q increases with an increase in the slip parameter β. The slip condition allows partial relative motion between the fluid and the channel wall, unlike the classical no-slip condition. An increase in β reduces the shear resistance at the wall, enabling the fluid to move more freely. From a physical standpoint, enhanced slip weakens wall friction, which facilitates the flow and results in a higher volumetric flow rate.

It is evident from Fig.(8c)) that the volumetric flow rate Q decreases as the Jeffery fluid parameter λ_1 increases. The parameter λ_1 characterizes the viscoelastic nature of the Jeffery fluid, accounting for both viscous and elastic effects. Higher values of λ_1 enhance the elastic response of the fluid, increasing internal resistance to deformation. As a result, the flow is slowed down and

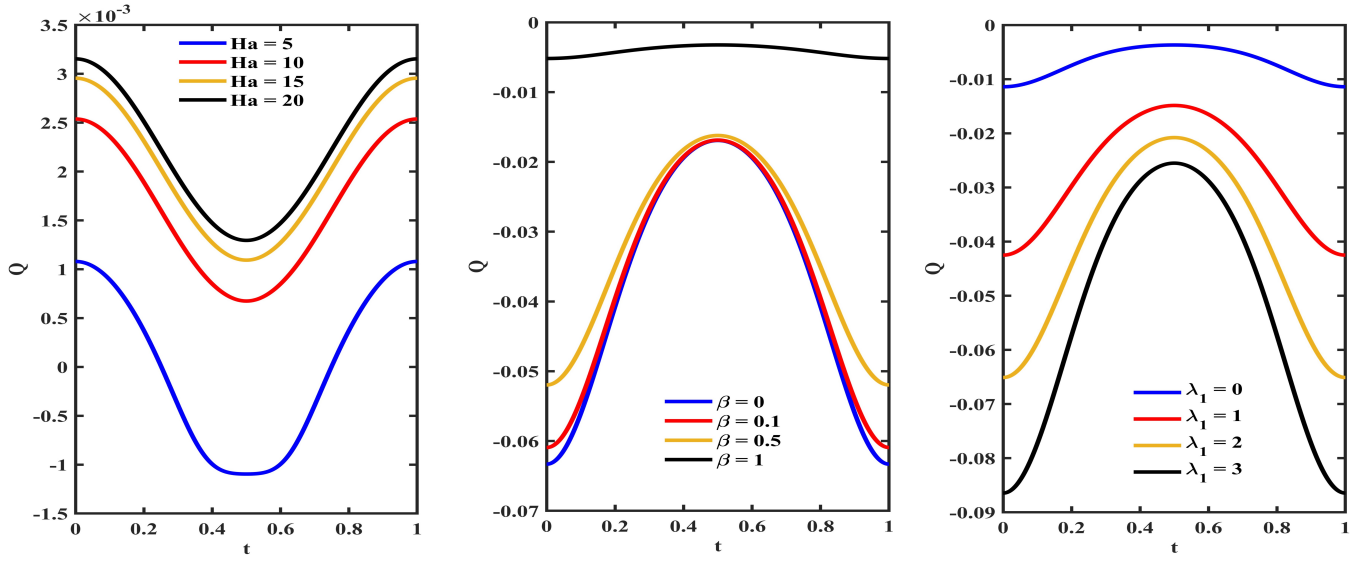

(a) (b) (c)

Figure 8: Volumetric flow rate for various value of (a) Hartmann number Ha, (b) slip parameter β and (c) Jeffery fluid parameter λ_1 at the compression phase with fixed values $x = 0.25$, and time $t = T/4$.

the volumetric flow rate decreases.

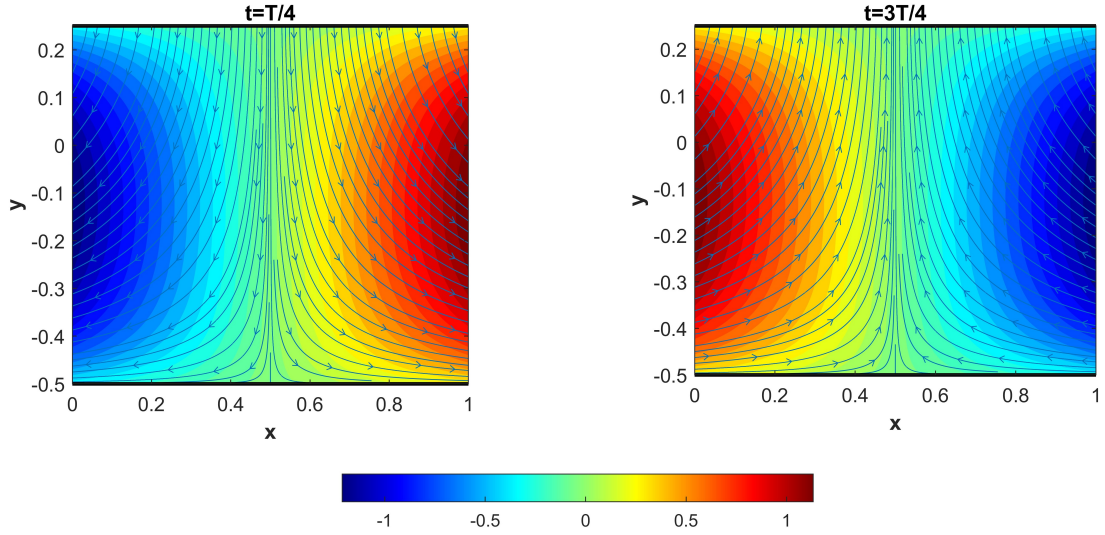

Figure 9: Contour plots of axial velocity and corresponding streamlines at $t = T/4$ and $t = 3T/4$ for $\beta = 0.1$ and $Ha = 5$, illustrating phase-dependent flow reversal and magnetic damping effects in the microchannel.

Fig. (9) shows axial velocity and streamline contours at $t = T/4$ and $t = 3T/4$ phases, with $\beta = 0.1$ and $Ha = 5$. A positive velocity region (red zone) emerges toward the right side of the

channel at $t = T/4$, indicating forward motion at the higher moving wall. The upper wall's cyclic movement causes flow recirculation on the left side, which has a matching reverse flow (blue zone). The streamlines confirm a weak channel vortex.

Oscillatory flows exhibit phase-shifted velocity distributions at $t = 3T/4$. Flow decelerates and reverses on the right side when the high-velocity zone shifts left. Due to the periodic driving mechanism, the two cases are symmetrical. The Lorentz force dampens velocity gradients and suppresses strong vortices, indicating the magnetic field ($Ha = 5$)'s influence. The low slip value ($\beta = 0.1$) effectively transfers momentum from the moving wall, preserving flow structures.

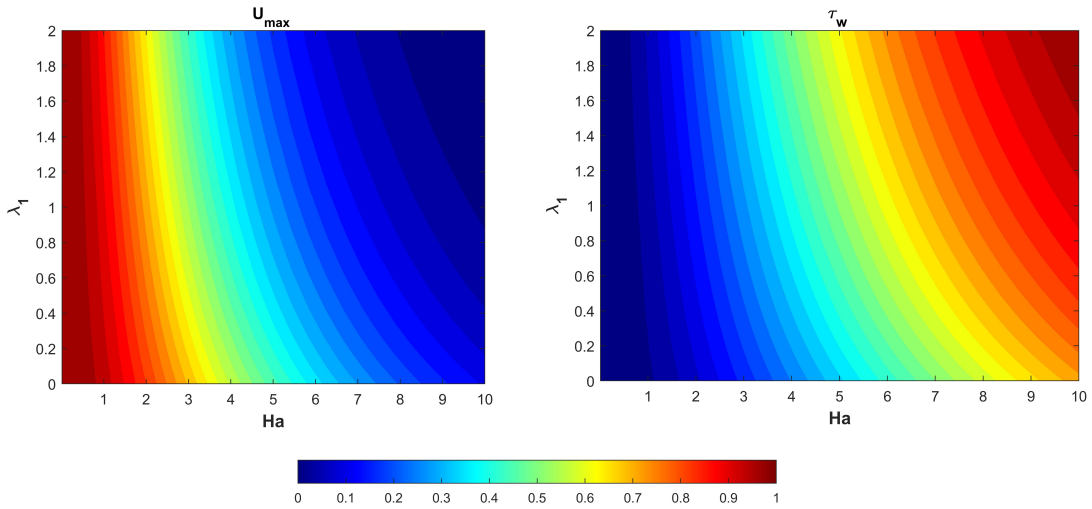

Figure 10: Contour plots of maximum velocity ($U_{\max}$) and wall shear stress (τ_w) at the upper wall showing the effects of Hartmann number (Ha) and Jeffrey parameter (λ_1) at $x = 0.25$ and $t = T/4$.

The figure (10) clearly demonstrates a sharp decrease in $U_{\max}$ as the Hartmann number Ha increases. The physical explanation for this phenomenon is the Lorentz force that is generated by the transverse magnetic field and acts as an opposing force to the flow, thereby reducing the velocity field. A larger reduction is observed for higher λ_1 values, indicating that magnetic damping is enhanced by fluid elasticity.

On the other hand, as Ha increases, the wall shear stress τ_w also increases. Sharper velocity gradients are observed close to the wall because core flow is suppressed by larger magnetic fields. In addition, the fact that τ_w increases as λ_1 does suggest that border resistance is amplified by viscoelastic processes.

Fig. (11) shows that the slip parameter β increases as $U_{\max}$ decreases. This design features a sliding top wall, which typically minimizes drag. However, in this case, slip weakens the driving

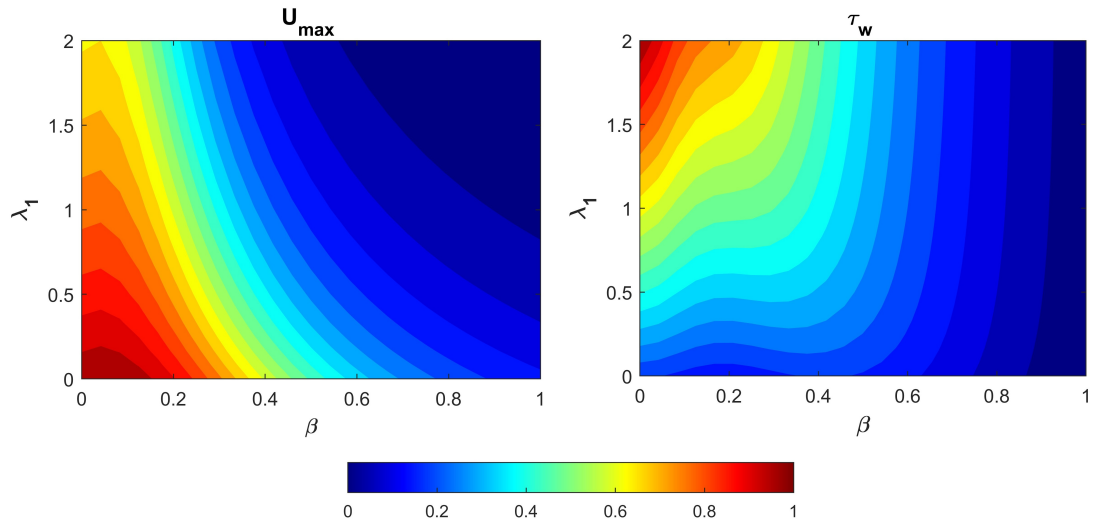

Figure 11: Contour plots of maximum velocity ($U_{\max}$) and wall shear stress (τ_w) at the upper wall illustrating the influence of slip parameter (β) and Jeffrey parameter (λ_1) at $x = 0.25$ and $t = T/4$.

effect and lowers peak velocity by reducing momentum transfer from the wall to the fluid.

Further, for an increase in β, τ_w decreases due to the physical consistency of slip reducing the velocity gradient near the wall. At low β, a larger λ_1 raises U_{max} and τ_w, but this effect diminishes as slip takes over.

4. Conclusions

This work examines slip magnetohydrodynamic flow of a Jeffrey fluid in a microchannel featuring a moving top wall and a stationary lower wall, utilizing lubrication theory. Analytical formulae have been derived for velocity components, shear stress, and pressure. The research indicates that the flow exhibits a pronounced periodic pattern, alternating between $t = T/4$ and $t = 3T/4$. The oscillatory motion of the upper wall predominantly influences the flow. The flow decreases with an increase in the Hartmann number (Ha) and the Jeffrey parameter (λ_1), while the wall shear stress (τ_w) increases due to heightened resistance and magnetic damping effects. As the Hartmann number increases, magnetic (Lorentz) damping causes a reduction in axial and vertical velocities. Further, shear stress decreases but pressure differential and gradient enhanced with an increase in Ha which stabilize flow. The slip parameter (β) substantially influences momentum transfer in the system by reducing wall-fluid interaction. This consequently leads to a decrease in both the maximum velocity (U_{max}) and the maximum shear stress (τ_w).

The study is in a good agreement with the study of Yasser Abolekassem [29] for Newtonian fluid and extend the results for the non-Newtonian fluid.

Funding

Financial support from the Council of scientific & Industrial Research (CSIR) to Mr. Anil Singh Negi in the form of a Senior Research Fellowship is gratefully acknowledged (Grant No. 09/1303(17040)/2023-EMR-I).

References

[1] A. M. Siddiqui, T. Haroon, and M. A. Rana, On the numerical solution of unsteady squeezing MHD flow of a second-grade fluid between parallel plates, *Advances in Studies Theoretical Physics*, 2012.

[2] N. Ullah, A. Khan, and M. Islam, Approximation of first grade MHD squeezing fluid flow with slip boundary condition, *Mathematical Problems in Engineering*, 2013.

[3] N. Ullah, A. Khan, and S. Shafie, Application of Daftardar–Jafari method to first-grade MHD squeezing flow with slip in porous medium, *Abstract and Applied Analysis*, 2014.

[4] N. Ullah, I. Khan, and S. Shafie, Analytical study of MHD squeezing flow of Casson fluid between parallel plates, *Cogent Mathematics*, 2016.

[5] J. Ahmed and M. J. Uddin, Effects of magnetic field on squeezing flow of Casson fluid between parallel plates, *Journal of King Saud University – Science*, 2017.

[6] A. S. Dogonchi and D. D. Ganji, Heat transfer of MHD nanofluid between parallel plates with unsteady squeezing, *Computational Methods in Applied Mechanics and Engineering*, 2016.

[7] S. Ghadikolaei, M. Yassari, and R. Sadeghi, Unsteady MHD Eyring–Powell squeezing flow: Heat and mass transfer with radiation, *Alexandria Engineering Journal*, 2017.

[8] K. Vajravelu, M. A. Imran, and S. U. Haq, Unsteady MHD flow and heat transfer of nanofluid between two parallel plates, *Journal of Molecular Liquids*, 2017.

[9] M. G. Sobamowo and M. O. Oke, MHD squeezing flow of nanofluid with velocity slip boundary conditions, *Results in Physics*, 2018.

[10] S. Ahmad, W. A. Khan, and M. I. Khan, Dual solutions for MHD squeezing flow of nanofluid, *AIP Advances*, 2018.

[11] D. Kumar, J. Prakash, and S. Prasad, MHD squeezing flow of Jeffrey fluid between parallel plates with slip effects, *Nonlinear Engineering*, 2018.

[12] B. K. Jha and B. A. Gwandu, MHD free convection in a vertical slit micro-channel with superhydrophobic slip and temperature jump, *SN Applied Sciences*, 2019.

[13] L. A. Lund, S. M. Hussain, and I. Khan, Viscous dissipation in MHD micropolar fluid with slip effects, *AIP Advances*, 2019.

[14] B. K. Jha and S. O. Salawu, Hall and ion-slip effects on MHD flow in a vertical microchannel, *Heat Transfer*, 2020.

[15] H. Cui, Y. Li, and X. Zheng, Transient MHD flow and heat transfer in a microchannel, *Physics of Fluids*, 2020.

[16] M. M. Noor, H. Khan, and Z. Abbas, Slip effects on MHD squeezing flow of Jeffrey nanofluid with chemical reaction, *Mathematics*, 2021.

[17] M. M. Noor, S. A. Hussain, and H. Khan, Effects of heat generation and chemical reaction on squeezing flow of Jeffrey fluid with slip, *PLOS ONE*, 2021.

[18] M. M. Noor, H. Khan, and Z. Abbas, Soret and Dufour effects on unsteady MHD Jeffrey squeezing flow through a permeable medium, *Scientific Reports*, 2022.

[19] J. An, F. Chen, and X. Wang, Electromagnetohydrodynamic flow of fractional viscoelastic fluids through a microchannel with Navier slip, *Applied Mathematics and Mechanics*, 2022.

[20] S. M. Hussain and A. Khan, Bio-thermal convection in MHD nanofluid with multiple slip conditions, *Alexandria Engineering Journal*, 2022.

[21] P. Kundu and S. Das, A review on electro-magnetohydrodynamic flows in microchannels, *Micromachines*, 2022.

[22] Y. Ma, W. Zhang, and Y. Chen, Electromagnetohydrodynamic flow in a microchannel with random wall roughness under slip and EDL effects, *Micromachines*, 2023.

[23] A. Akinshilo, O. D. Makinde, and B. O. Falodun, MHD flow of Casson nanofluid in a porous microchannel with slip and melting effects, *Thermal Science*, 2023.

[24] M. Saghafian and H. Rashidi, Unsteady natural-convection MHD slip flow in an open-ended vertical parallel-plate microchannel, *Scientific Reports*, 2024.

[25] M. Rehman, A. Khan, and S. Islam, Squeezing dynamics in Jeffrey fluids with Cattaneo–Christov heat flux and reactive flow, *ZAMM*, 2024.

[26] H. A. Al-Farhany and M. A. Ramadan, Entropy generation in thermosolutal MHD slip flow through inclined microchannels, *ZAMM*, 2024.

[27] A. Yasser and S. Abdelaziz, Electro-osmotic and MHD slip flow with wall motion in microchannels, *Physica Scripta*, 2024.

[28] B. Singh and A. Sharma, Hall and ion-slip effects on MHD squeezing flow of nanofluids with entropy generation, *Advances in Mechanical Engineering*, 2024.

[29] Aboelkassem, Y., Alouh, M., & Aluko, O. (2025). Magnetohydrodynamics slip flow in a microchannel with moving walls. Physics of Fluids, 37(7).